Influence of FtsZ GTPase activity and concentration on nanoscale Z-ring structure *in vivo* revealed by three-dimensional superresolution imaging

Zhixin Lyu, Carla Coltharp, Xinxing Yang, Jie Xiao

Department of Biophysics and Biophysical Chemistry, Johns Hopkins School of Medicine, Baltimore, Maryland, United States of America

This article has been accepted for publication and undergone full peer review but has not been through the copyediting, typesetting, pagination and proofreading process which may lead to differences between this version and the Version of Record. Please cite this article as an 'Accepted Article', doi: 10.1002/bip.22895

Abstract

FtsZ is an essential bacterial cytoskeletal protein that assembles into a ring-like structure (Z-ring) at midcell to carry out cytokinesis. *In vitro,* FtsZ exhibits polymorphism in polymerizing into different forms of filaments based on its GTPase activity, concentration, and buffer condition. *In vivo*, the Z-ring appeared to be punctate and heterogeneously organized, although continuous, homogenous Z-ring structures have also been observed. Understanding how the Z-ring is organized *in vivo* is important because it provides a structural basis for the functional role of the Z-ring in cytokinesis. Here, we assess the effects of both GTPase activity and FtsZ concentration on the organization of the Z-ring *in vivo* using three-dimensional (3D) superresolution microscopy. We found that the Z-ring became more homogenous when assembled in the presence of a GTPase-deficient mutant, and upon overexpression of either wt or mutant FtsZ. These results suggest that the *in vivo* organization of the Z-ring is largely dependent on the intrinsic polymerization properties of FtsZ, which are significantly influenced by the GTPase activity and concentration of FtsZ. Our work provides a unifying theme to reconcile previous observations of different Z-ring structures, and supports a model in which the wt Z-ring comprises loosely associated, heterogeneously distributed FtsZ clusters.

Introduction

In bacteria, the cytokinetic machinery is built upon a polymeric scaffold formed by the FtsZ protein.[1] Polymeric FtsZ filaments coalesce into a 'Z-ring' at midcell to recruit other division proteins[1] and possibly guide the formation of the division septum.[2] *In vitro,* FtsZ filaments from *Escherichia coli* are typically single-stranded and 100 - 200 nm in length.[3-5] With the addition of crowding agents or membrane anchoring, these short filaments can form extended filaments that bundle or curl into helices and toroids.[6-9]

Electron cryotomography (ECT) studies in *Caulobacter crescentus* initially supported an *in vivo* Z-ring structure that comprised mostly short, scattered single-stranded filaments of FtsZ.[10] However, recent ECT studies in *C. crescentus* and *E. coli* are more consistent with the existence of long, continuous FtsZ filaments that wrap multiple times around the circumference of the cell division site.[9] At the same time, superresolution fluorescence microscopy has produced mounting evidence that the Z-ring is not continuous, but instead exhibits a clustered morphology in many bacterial species.[11-18] This clustered morphology is supported by superresolution imaging of other proteins that localize to the Z-ring[15,16] and immuno-fluorescence imaging of native FtsZ.[13,15,17-19]

Previously, we proposed that the Z-ring may sample both continuous and discontinuous configurations because of its continual remodeling by subunit turnover.[17] It is known that GTP hydrolysis promotes the fracture of long FtsZ polymers *in vitro*[20] and stimulates Z-ring subunit turnover *in vivo*.[21] Thus, a more continuous Z-ring organization could be favored by conditions of low GTPase activity. Additionally, long, continuous FtsZ filaments arranged orderly along the

waist of the cell may offer higher contrast to be detected in the most recent ECT study than short, heterogeneously organized FtsZ filaments.[9]

Here, we directly assessed the effects of FtsZ GTPase activity on Z-ring organization by quantitatively comparing the Z-ring structure formed by wild-type (wt) FtsZ with that formed by a severe FtsZ GTPase mutant D212A using three-dimensional (3D) superresolution imaging. The D212 residue is highly conserved in FtsZ sequences across different bacterial species and is considered to be part of the catalytic T7 loop responsible for GTP hydrolysis.[22,23] The D212A mutation leads to a reduction of GTPase activity to ~ 7% of wt and to a deficiency in polymerization *in vitro* in the absence of the bundling reagent Ca^{2+}.[24] *In vivo,* the D212A mutant is unable to support cell division in the absence of wt FtsZ at restrictive temperatures,[25] but in the presence of wt FtsZ, cells harboring ectopically expressed $FtsZ^{D212A}$ mutant are able to divide, although often with abnormal septa and cell shape.[25]

By comparing 3D superresolution images of Z-ring structures formed by $FtsZ^{wt}$ or $FtsZ^{D212A}$ expressed at similar levels, we found that mutant Z^{D212A}-rings were significantly more homogenous than wt Z-rings. Furthermore, largely continuous Z-ring structures were observed not only when the $FtsZ^{D212A}$ mutant, but also when the wt FtsZ protein was overexpressed at a level of ~ 8-fold of the endogenous wt FtsZ concentration. Thus, our results suggest that the GTPase activity and concentration of FtsZ play important roles in organizing Z-ring structure. These experiments support our previous Z-ring organization model in which the wt Z-ring is normally composed of loosely associated, heterogeneously distributed FtsZ clusters.[11,13,16,17]

Materials and methods

Bacterial strains and plasmids

The *E. coli* strain HST08 (Clontech Laboratories, Inc) was used for cloning. The *E. coli* strain BW25113[26] was used as the background strain for the expression of FtsZ or FtsZ-fusion proteins and imaging.

The pJL005 ($P_{T5\text{-}lac}$::FtsZ^{wt}-mEos3.2) plasmid was constructed from the pJB106 ($P_{T5\text{-}lac}$::FtsZ-mEos3.2)[13] plasmid as follows. Three nucleotides ACT were inserted into the space between the T5 promoter and the start codon of the *ftsZ* gene using the QuikChange protocol (Agilent) with primers 1 and 2 (Table S1), to achieve a lower translation efficiency and thus lower expression level of FtsZ^{wt}-mEos3.2. The pJL006 ($P_{T5\text{-}lac}$::FtsZ^{D212A}-mEos3.2) plasmid was constructed from the pJL005 ($P_{T5\text{-}lac}$::FtsZ^{wt}-mEos3.2) plasmid using the QuikChange protocol (Agilent) with the primers 3 and 4 (Table S1) to mutate the nucleotide sequence encoding for D212A. The pXY180 (P_{BAD}::FtsZ^{wt}) plasmid was constructed by amplifying the wt *ftsz* gene from pJB066 (P_{BAD}::FtsZ-PAmCherry1)[16] using primers 3 and 4 (Table S1). The amplified product was restricted with NheI and SalI, then ligated into similarly-digested pJB066 to create pXY180 (P_{BAD}::FtsZ^{wt}). The pJL012 (P_{BAD}::FtsZ^{D212A}) plasmid was constructed from the pXY180 (P_{BAD}::FtsZ^{wt}) plasmid using the QuikChange protocol (Agilent) with the primers 5 and 6 (Table S1) to mutate the nucleotide sequence encoding for D212A. The pJB153 ($P_{T5\text{-}lac}$::mEos3.2-ZapA) plasmid was constructed by amplifying the *mEos3.2* gene from pTriEX-HM-mEos3 (a gift from J. Yu) using primers 7 and 8 (Table S1). The amplified product was restricted with SpeI and SphI, then ligated into the similarly-digested pJB051 ($P_{T5\text{-}lac}$::mEos2-ZapA)[16] to generate pJB153 ($P_{T5\text{-}lac}$::mEos3.2-ZapA).

The constructed plasmids pJL005 and pJL006 were then individually transformed into BW25113 cells and maintained with appropriate antibiotic selection (chloramphenicol, 150 μg/ml). The plasmid pairs pJL005 and pXY180, pJL006 and pJL012, pJL005 and pJB153 were transformed sequentially into BW25113 cells and maintained with appropriate antibiotic selection (chloramphenicol, 150 μg/ml; spectinomycin, 100 μg/ml).

Growth conditions and media

Liquid cultures of BW25113 strains harboring different plasmids were grown at 37°C in Luria-Bertani (LB) medium overnight to reach the stationary phase. Cultures were then diluted 1:200 in M9 medium supplemented with 0.4% glucose, 1 × MEM vitamins and 1 × amino acids (Sigma) and grown at room temperature (RT) until the OD_{600} reached 0.2~0.3. For cells harboring a single plasmid, 20 μM or 80 μM IPTG was added to the cultures to induce the expression of FtsZ fusion proteins for 2 hrs at RT. The OD_{600} was kept ~ 0.3 during the induction. After induction, cells were pelleted gently, resuspended in the same volume of fresh M9 supplemented medium without IPTG, and allowed to grow at RT for 2 hrs before proceeding to Western blot or PALM imaging. This outgrowth period allowed additional time for mEos3.2 to mature, and also reduced the cellular levels of overexpressed FtsZ-mEos3.2 fusion protein by cell division. At the end of the 2-hr outgrowth period the OD_{600} of cells were ~ 0.5-0.6. For strains harboring two plasmids, cells were harvested by centrifugation and resuspended in fresh M9 medium supplemented with 0.4% glycerol. 0.4% or 1.0% Arabinose was added to the culture to induce the expression of FtsZ proteins from pXY180 (P_{BAD}::$FtsZ^{wt}$) or pJL012 (P_{BAD}::$FtsZ^{D212A}$) plasmids. Cells were allowed to grow with shaking for 1 hr at RT followed by centrifugation. Pellets were

washed twice and resuspended in the same volume of fresh M9 medium supplemented with glucose. 20 μM IPTG was added to the cultures to induce the expression of FtsZ or ZapA fusion proteins from pJL005 ($P_{T5\text{-}lac}$::$FtsZ^{wt}$-mEos3.2), pJL006 ($P_{T5\text{-}lac}$::$FtsZ^{D212A}$-mEos3.2) or pJB153 ($P_{T5\text{-}lac}$::mEos3.2-ZapA) plasmids. Cells were allowed to grow with shaking for 2 hrs at RT followed by centrifugation. Pellets were washed twice and resuspended in the same volume of fresh M9 medium supplemented with glucose. Cells grew for further 2 hrs without IPTG at RT before proceeding to Western blot or PALM imaging.

Quantifying FtsZ concentration in single cells

To quantify total cellular FtsZ concentrations in individual cells, we used a previously established procedure to convert integrated green fluorescence of $FtsZ^{wt}$-mEos3.2 and $FtsZ^{D212A}$-mEos3.2 into protein numbers.[11,13] In this procedure, we first used Western blot to measure the average protein expression levels of endogenous $FtsZ^{wt}$, $FtsZ^{wt}$-mEos3.2, or $FtsZ^{D212A}$-mEos3.2 under different induction conditions (Figure S1). Cells were grown and harvested as described above. Cells were divided into two batches, one for Western blot, and one for superresolution imaging. For Western blot, we counted cell numbers of each sample using a Petroff-Hausser counting chamber and loaded the lysate of the same number of cells of each sample onto a polyacrylamide gel (Figure S1A-B). In addition to cell samples, different amounts of purified $FtsZ^{wt}$ and $FtsZ^{wt}$-mEos2 were loaded onto the same gel to construct a standard curve (Figure S1Aii-iii) for concentration calculation and to calibrate for small differences in transfer and staining efficiencies due to different molecular weights between FtsZ and FtsZ-mEos2.[13]

Western blotting was conducted as previously described[13] using an antibody against FtsZ (a gift from H. Erickson). To calibrate small differences in the number of cells loaded into each lane, we also used an antibody against the endogenous bacterial elongation factor Tu (EF-Tu, Hycult Biotech Inc) as an internal standard. We ran each set of samples on two identical gels and transferred to two different blot membranes because of the similar molecular weights of FtsZ (40 kDa) and EF-Tu (43 kDa). The number of cells loaded into each lane was then calibrated using measured EF-Tu band intensity normalized against the corresponding cell length. This latter normalization was performed because we observed that cells induced with 80 μM IPTG were significantly longer than those induced with 20 μM IPTG (Figure S1Bii) and the larger cells have higher amounts of EF-Tu (Figure S1Ai, S1Bi). To do so we first divided the measured EF-Tu band intensity in each lane against the corresponding averaged cell length to normalize for different cell sizes, then further normalized against the EF-Tu/cell-length value of the $FtsZ^{wt}$ 20 μM IPTG condition to obtain a calibration factor for cell numbers loaded into each lane. The actual number of cells loaded in each lane was then calculated by multiplying this calibration factor for each lane with the number of cells counted for the $FtsZ^{wt}$ 20 μM IPTG condition.

To calculate the absolute amounts of cellular FtsZ and FtsZ-mEos3.2 loaded into each lane, we measured the intensity of the corresponding band and compared with the standard curve constructed using the corresponding purified protein (Figure S1Aii-iii). This amount was then divided by the corresponding number of cells loaded into each lane to obtain the average number of FtsZ or FtsZ-mEos3.2 per cell. This experiment was repeated three times, and the average values were reported in Figure S1Biii. The values of endogenously expressed $FtsZ^{wt}$ are

consistent with those that we and others have published before (3,000 - 6,000 molecules/cell).[11,13,27-30]

To assess the concentration of FtsZ in individual cells imaged by superresolution, we measured the integrated fluorescence of each cell (I^i) in the green channel before photoactivating mEos3.2 to emit red fluorescence for PALM imaging. We divided the average number of FtsZ-mEos3.2 molecules per cell $\langle N_m \rangle$ measured by Western blot by the averaged integrated green fluorescence $\langle I \rangle$ to obtain the conversion factor α between fluorescence and FtsZ-mEos3.2 molecule numbers. The total number of FtsZ-mEos3.2 molecules (N_m^i) expressed in this individual cell *i* was then calculated by

$$N_m^i = \alpha I^i$$

Assuming that the endogenous wt FtsZ concentration is constant in individual cells under each induction condition, the total cellular FtsZ concentration [FtsZ-mEos3.2 + FtsZ] expressed in units of the endogenous wt FtsZ concentration (WTC) of cell i can be described as below:

$$\mathrm{WTC}^i = \frac{\left(N_m^i + \langle N_Z \rangle\right) / \langle L \rangle}{\langle N_Z^{20\mu\mathrm{M}} \rangle / \langle L^{20\mu\mathrm{M}} \rangle}$$

Where $\langle N_Z \rangle$ is the average number of endogenous FtsZ^{wt} molecules per cell under this condition measured by Western blot (Figure S1A-B); $\langle L \rangle$ is the average cell length under the same condition; $\langle N_Z^{20\mu\mathrm{M}} \rangle$ is the average number of endogenous FtsZ^{wt} under the 20 μM IPTG induction of FtsZ^{wt}-mEos3.2 measured by Western blot; and $\langle L^{20\mu\mathrm{M}} \rangle$ is the average length of cells under the 20 μM IPTG induction of FtsZ^{wt}-mEos3.2. Note here that by dividing by the

corresponding cell lengths under different induction conditions, we effectively measured the concentration of total cellular FtsZ rather than the absolute number of FtsZ molecules per cell.

3D PALM imaging

Cells harboring different plasmids were prepared as described above and were added to an agarose pad (3% in M9 medium) laid in an observation chamber (FCS2, Bioptechs). The chamber was locked on the microscope stage (ASI, Eugene, OR) to minimize mechanical drifts. PALM imaging was performed on an Olympus IX71 inverted microscope with a 100 ×, 1.49 NA oil-immersion objective. The green state of mEos3.2 before activation was excited at 488 nm with laser intensity 40 W/cm^2 to obtain integrated green fluorescence intensity of individual cells, which was used to quantify FtsZ concentration as described above. mEos3.2 was then switched to the red-emitting state using a 405 nm laser with intensity increased stepwise from 0 to 12 W/cm^2 to compensate for the gradually depleted pool of unactivated mEos3.2. The activated red mEos3.2 was excited at 568 nm continuously, with laser intensity of 1.6 kW/cm^2 and exposure time of 10 ms. Typically, ~7000 frames were acquired before most mEos3.2 molecules were photobleached. Both green- and red-channel fluorescence were collected by the same dual-band emission filter (ET F/Cy3M, Chroma Technology), before acquisition by an EMCCD camera (iXon Ultra 897, Andor Technology). All the lasers and the EMCCD camera were controlled by the MetaMorph software (Molecular Devices).

For the 3D PALM imaging, a cylindrical lens (Thorlabs Inc) with 700 mm focal length was placed in the microscope emission pathway to introduce astigmatism to the single-molecule PSF.[31] The position of the cylindrical lens was adjusted to achieve optimal astigmatism. TetraSpeck

fluorescent microspheres with average diameter 0.1 μm (Invitrogen Molecular Probes) were used to calibrate the z-dependent changes to the shape of the astigmatic PSF. The xy positions were determined through the 2D Gaussian fitting of the PSF, while the z position was given by the calibration curve obtained by z-scanning of the fluorescent microspheres.[31] Because of the refractive index mismatch between the transmission path of the microspheres used for calibration (glass and oil) and that of the fluorescent proteins (aqueous cell environment, glass, and oil), the z values obtained from the calibration curve were rescaled by a factor of 0.75.[32] The measurements of ring dimensions were achieved by custom MATLAB software described previously.[17] To quantitatively compare with previously reported dimensions obtained under different spatial resolutions, Z-ring dimensions here were deconvolved as described.[17] Both apparent and deconvolved dimensions were listed in Table S2.

Results

Validation of 3D, live-cell PALM imaging using astigmatism and an FtsZ-mEos3.2 fusion protein

To compare quantitatively Z-ring structures formed by wt FtsZ and the D212A mutant, we first performed 3D superresolution imaging on wt FtsZ fused to a truly monomeric photoactivatable fluorescent protein (PA-FP) mEos3.2[33] using cylindrical lens-induced astigmatism.[31] We ectopically expressed $FtsZ^{wt}$-mEos3.2 fusion protein in BW25113 cells, used a combination of Western blot and the green fluorescence intensity of mEos3.2 to sort cells based on their total cellular FtsZ concentrations (including both tagged and untagged FtsZ,

Material and Methods, Figure S1, Figure 2B), and analyzed cells that have ~ 3-fold of endogenous, wt FtsZ concentration (WTC). Under our imaging condition we obtained a spatial resolution of ~50 nm in xy and ~80 nm in z (Figure S2). In Figure 1Ai we show representative 3D PALM images of live *E. coli* BW25113 cells ectopically expressing $FtsZ^{wt}$-mEos3.2. The overall dimensions (Figure 1B, Table S2, width = 84 ± 2 nm; thickness = 47 ± 2 nm, *n* = 126; deconvolved from achieved spatial resolutions) and the clustered appearance of the Z-ring are similar to what we previously observed in fixed cells using an $FtsZ^{wt}$-mEos2 fusion imaged using interferometric PALM (iPALM),[17] and are in agreement with Z-ring structures observed in other bacterial species.[12,14] Moreover, when we sorted individual cells by their Z-ring diameters to generate a pseudo time lapse representing the constriction process, we observed essentially the same trend as we and others previously reported[14,17] — both the width and thickness of the Z-ring remained constant throughout constriction, and there was no significant structural reorganization of the Z-ring during constriction (Figure S3A). Finally, when we ectopically expressed an mEos3.2-ZapA fusion protein in wt cells producing only endogenous, unlabeled FtsZ (BW25113) and imaged ZapA-rings under the same condition, we observed essentially the same clustered, heterogeneously organized morphology of mEos3.2-ZapA rings (Figure S4Ai). As ZapA associates with FtsZ,[16,34,35] and has been previously used as a reliable marker for Z-ring position and organization,[17,36,37] this experiment, together with other characterizations described above, validate our new 3D, live-cell PALM imaging method and the use of the new PA-FP mEos3.2 as a reliable fusion tag for FtsZ.

Z^{D212A}-rings are wider and more homogenously organized compared to Z^{wt}-rings

Next, we ectopically expressed an FtsZ^{D212A}-mEos3.2 fusion protein in the wt BW25113 cell background at a similar level (Materials and Methods, Figure S1) as that of the FtsZ^{wt}-mEos3.2 fusion (~ 3 WTC, Table S2), and imaged the corresponding Z^{D212A}-ring structure under the same imaging condition. As shown in Figure 1Aii, qualitatively Z^{D212A}-rings exhibited a more homogenous distribution compared to the Z^{wt}-rings (Figure 1Ai). The averaged thickness of Z^{D212A}-rings was indistinguishable from that of wt Z-rings (46 ± 2 nm, *n* = 89, Figure 1Bii, Table S2), but its width is slightly larger (93 ± 3 nm, Figure 1Bi, Table S2), with more cells having considerably wider rings in the range of 120 - 140 nm. Despite this change, the pseudo time-lapse of Z^{D212A}-rings during cell constriction showed constant width and thickness (Figure S3B), as observed for Z^{wt}-rings (Figure S3A).

To quantitatively compare the distributions of FtsZ clusters in Z^{wt}- and Z^{D212A}-rings, we used a previously established autocorrelation analysis.[17] In this analysis, all FtsZ molecules in the ring are projected along the circumference of the ring. The spatial autocorrelation function (ACF) is calculated as the apparent probability distribution of distances between all molecule pairs. If all FtsZ molecules in the ring are homogenously distributed, the resulting ACF curve is flat with a constant value of unity across all distance ranges. In Figure 1C we show that the ACF curves calculated for the wt and D212A mutant Z-rings were significantly different from each other. The ACF of Z^{wt}-rings had a significantly higher correlation value at short distances, with a characteristic decay length at half maximum of ~ 70 nm. In contrast, the ACF of Z^{D212A}-rings had a lower correlation value at short distances, but a longer characteristic decay length of ~ 90 nm. This comparison suggests that FtsZ clusters in the mutant Z^{D212A}-ring are larger and more homogenously distributed than those in the Z^{wt}-ring. ACF curves calculated for mEos3.2-ZapA

rings showed a comparable characteristic decay length to that of Z^{wt}-rings (Figure S4C), confirming the significant difference between Z^{wt}- and Z^{D212A}-rings.

Z-ring structure is dependent on FtsZ expression level

Previously we proposed that the Z-ring is composed of loosely-associated, heterogeneously-distributed FtsZ clusters confined in a toroid zone of ~ 100 x 60 nm at the midcell.[11,16,17] This model is supported by the calculation that there are not enough FtsZ molecules to fully occupy the toroid zone if they were tightly aligned with each other,[11] and also by the observation that in 2D PALM imaging the width of the Z-ring does not increase significantly with increased FtsZ expression level up to 8-fold of WTC, likely because the empty space in the ring can accommodate additional FtsZ molecules without appreciable expansion of the ring volume.[11]

To examine whether this model still holds for the $FtsZ^{D212A}$ mutant, we further overexpressed $FtsZ^{D212A}$-mEos3.2 in wt BW25113 cells to achieve a final total cellular FtsZ concentration at 5 to 11 WTC (Material and methods, Figure S1, Figure 2B), and compared the resulting mutant Z-ring structures with those formed by $FtsZ^{wt}$-mEos3.2 at similar expression levels. Strikingly, as shown in Figure 2A, the apparent appearance of the rings became gradually more homogenous when the expression level increased. Perhaps most importantly, at each comparable expression level, Z^{D212A}-rings (Figure 2A bottom panel) adopted smoother distributions of FtsZ clusters inside the ring than the corresponding Z^{wt}-rings (Figure 2A top panel), with the mutant Z^{D212A}-rings becoming largely continuous at the highest expression level (~ 11 WTC). These observations were further supported by comparison of the ACF curves of

Z^{wt}- and Z^{D212A}-rings (Figure 2Bii-iii). For cells expressing similar total cellular FtsZ levels but either wt or the D212A mutant (Figure 2Bii-iii), ACF curves of Z^{D212A}-rings (red) had lower correlation values and longer decay lengths than those of Z^{wt}-rings (black); for cells expressing the same type of FtsZ but with different levels, higher expression levels led to flatter ACF curves (2Bii-iv, markers of same color but different shapes). At the highest expression level of the Z^{D212A}-ring (~ 11 WTC), the corresponding ACF curve approached that of a Z-ring with randomly, homogenously distributed FtsZ molecules (Figure 2Biv, compare red diamond with the gray curve). Note that when we overexpressed untagged wt FtsZ or $FtsZ^{D212A}$ instead of mEos3.2-labeled fusions to reach a total level of overexpression at ~6 WTC, we observed the same trend that both Z^{wt}-rings and Z^{D212A}-rings became more homogenously distributed (Figure S5A), with the ACF curve of Z^{D212A}-rings having lower correlation values and longer decay lengths than those of Z^{wt}-rings (Fig. S5C). This result demonstrates that the homogenous organization of the Z-ring is caused by overexpression of FtsZ rather than the mEos3.2 moiety, and that the decreased GTPase activity of $FtsZ^{D212A}$ likely further amplifies this effect.

Most interestingly, when we plotted the width and thickness of individual rings according to their expression levels (Figure 2C), we found that the width and thickness of the Z^{wt}-ring did not show appreciable concentration-dependence (Figure 2C, black dots), consistent with what we observed previously.[11] However, the width of the Z^{D212A}-ring increased significantly at higher concentrations, with the averaged ring width at ~ 160 nm at the highest expression level (~ 11 WTC) (Figure 2C, red dots). Overexpressing untagged $FtsZ^{D212A}$ at ~ 6 WTC level also led to significantly wider Z^{D212A}-rings when compared to Z^{wt}-rings (Fig. S5Bi). Taken

together, these results demonstrate that the dimension of the Z-ring is also likely influenced by the decreased GTPase activity of $FtsZ^{D212A}$.

Discussion

The FtsZ protein, a tubulin homolog and GTPase, exhibits polymorphism *in vitro* in forming polymers of different lengths, curvatures, shapes, and degrees of lateral interactions depending on a variety of buffer conditions.[6-8] As such, the precise structural organization of the Z-ring formed by FtsZ polymers *in vivo* has remained controversial. Early ECT and fluorescence-based superresolution studies showed that the Z-ring is discontiguous; individual FtsZ clusters, likely composed of multiple short FtsZ filaments, are randomly scattered and loosely confined in a narrow toroid zone at the midcell.[10-17,19] In contrast, a recent ECT study found that FtsZ forms long, continuous filaments wrapping around cell waist.[9]

Understanding how the Z-ring is organized *in vivo* is important because it provides a structural basis for the functional role of the Z-ring in cytokinesis. We previously hypothesized that different Z-ring organizations observed in different studies may reflect the ability of FtsZ's GTPase activity to modulate its polymerization.[17] It is known that the polymerization of FtsZ is stimulated by nucleotide binding at the monomer-monomer interface of an FtsZ filament, which constitutes the GTP binding pocket,[22] while the stochastic hydrolysis of GTP leads to a high chance for the protofilament to break at the site of hydrolysis.[20] Thus, a GTP-binding competent but GTP hydrolysis-incompetent mutant could form longer, much more stable

polymers than FtsZ^{wt}, possibly explaining why long, continuous FtsZ protofilaments became more apparent by ECT when the FtsZ^{D212A} mutant was over-expressed.[9]

To examine this hypothesis, in this work we used 3D superresolution imaging to compare quantitatively Z-ring structures formed by wt FtsZ and the FtsZ GTPase mutant D212A *in vivo*. The D212A mutation is part of the T7 loop responsible for GTP hydrolysis,[22,23] and corresponds to the synergy loop mutant E254A of α-tubulin, which is resistant to disassembly from microtubules.[38] This is also the same mutant used in the ECT study that observed long, continuous FtsZ filaments at midcell.[9] We found that, at the same expression levels, Z^{D212A}-rings appeared much more smooth and homogenous than Z^{wt}-rings (Figures 1A and 2A); this qualitative observation was further supported by the quantitative comparison of the corresponding ACF curves (Figure 1C and Figure 2B). These results suggest that the polymerization of FtsZ^{D212A} is indeed different from that of FtsZ^{wt} *in vivo*, and that this difference may partially explain the discrepancy between Z-ring organizations observed in previous studies. Note that we expressed the D212A mutant in the presence of endogenous FtsZ^{wt} to obtain comparable images. Nevertheless, even in the presence of FtsZ^{wt}, which should contribute significantly to the fracture of long FtsZ^{D212A} filaments, we still observed much more homogenously distributed and larger FtsZ clusters in the mutant strain compared to the wt strain. These results suggest that GTPase activity may indeed play an important role in determining the organization of the Z-ring. Note here that while GTPase deficiency is the dominant defect of D212A, we cannot rule out another possibility that the altered organization of FtsZ^{D212A}-rings could also be caused by some other unknown defects of the D212A mutant, such as altered lateral interactions between FtsZ filaments or with other FtsZ binding partners.

Further investigations exploring a large range of FtsZ mutants with different GTPase activities and/or deficiencies in FtsZ's interactions with itself and other divisome proteins will provide additional insight into this question.

A second finding from our work is that the total cellular concentration of FtsZ apparently influences the Z-ring organization as well. As shown in Figure 2A, the Z^{wt}-ring structure gradually transitioned from a clustered, heterogeneously organized ring to a smoother, more homogenous ring when the expression level of FtsZ increased. Z^{D212A}-rings exhibited the same trend, although they appear much smoother than Z^{wt}-rings at all comparable expression levels. At the highest expression level (~ 11 WTC), Z^{D212A}-rings appeared to be continuous structures with few gaps detected. These observations are supported by the corresponding quantitative comparisons between their ACFs (Figure 2B). Note that the gradual transition of Z^{wt}-rings was not obvious in our first study of Z-ring structure using 2D PALM imaging,[11] because when projected down to a 2D imaging plane individual FtsZ clusters overlapped significantly at high expression levels. Furthermore, the gradual transition to a smoother Z-ring is not due to increased sampling frequencies of the Z-ring structure at higher expression levels of FtsZ-mEos3.2, because at even the lowest expression level we used, the labeling density is ~ 3100 molecules/μm^2, corresponding to a Nyquist resolution of ~ 36 nm (Figure S2Biv), better than our experimental spatial resolution (~ 50 nm in x and y, Figure S2). This conclusion is supported by a simulation, in which we computationally decreased the number of FtsZ-mEos3.2 localizations at high expression levels to match that at low expression levels, we still observed a more homogenous distribution of FtsZ inside the Z-rings (Figure S6, compare rows ii and iii). Furthermore, our control experiments in which we overexpressed untagged FtsZ instead of

FtsZ-mEos3.2 fusions showed essentially the same results (Figure S5). Hence our imaging is not limited by labeling density, a common concern in single-molecule localization based superresolution imaging [39], and is likely not an artifact of the mEos3.2 fusion.

How does FtsZ expression level influence the overall Z-ring structure? We propose that increasing the concentration of FtsZ results in Z-ring homogenization in the same manner that expressing the GTPase-deficient D212A mutant does. Both perturbations result in an overall increase in the degree of FtsZ polymerization in the cell and in the Z-ring. This increased FtsZ density in the ring could in turn inhibit GTP hydrolysis activity,[29] further enhancing the formation of long or bundled FtsZ filaments in the Z-ring. Thus, modulating the GTPase activity and concentration of FtsZ may be two ways of ultimately regulating Z-ring homogeneity by influencing the degree of FtsZ polymerization.

The increased Z-ring homogeneity upon increased FtsZ concentration is consistent with our previously proposed model of the Z-ring as a loose structure with much unoccupied space between FtsZ clusters. Excess FtsZ molecules resulting from overexpression would naturally fill in the Z-ring gaps and lead to a more homogenously distributed ring structure with unchanged overall dimensions. This gap-filling model is consistent with the largely unchanged width of Z^{wt}-rings, and thickness of both Z^{wt} and Z^{D212A} rings, upon FtsZ overexpression, but does not explain our observation that the width of Z^{D212A}-rings increased substantially from ~ 90 nm to ~ 160 nm upon $FtsZ^{D212A}$ overexpression (Figure 2C). This increased width of Z^{D212A}-rings could not be a simple consequence of too many $FtsZ^{D212A}$ molecules to be accommodated in the limited space of the toroid zone at midcell when overexpressed. This is because at the same expression

levels, Z^{D212A}-rings showed similar midcell localization percentages compared to Z^{wt}-rings (Figure S3), thus the total number of $FtsZ^{D212A}$ molecules in the Z^{D212A}-ring should be similar to that of $FtsZ^{wt}$ in the Z^{wt}-rings, unlikely exceeding space available in the Z-ring.

We suggest that the different response of the width of Z^{D212A}-rings and Z^{wt}-rings upon FtsZ overexpression may reflect functional differences between $FtsZ^{wt}$ and $FtsZ^{D212A}$. In addition to its effect on the overall degree of FtsZ polymerization, the D212A mutation may also cause differences in the form or morphology of $FtsZ^{D212A}$ filaments relative to those of $FtsZ^{wt}$ in the Z-ring, as observed *in vitro*[24]. A likely possibility is that the GTPase deficiency of $FtsZ^{D212A}$ reduces the fraction of GDP-bound subunits in Z^{D212A}-rings compared to Z^{wt}-rings. Since GDP-bound FtsZ exhibits a higher degree of curvature than GTP-bound FtsZ,[40] this reduction in GDP occupancy would result in $FtsZ^{D212A}$ filaments that are less curved than those in Z^{wt}-rings. This change in curvature would in turn alter the orientational preference of $FtsZ^{D212A}$ filaments such that they may grow in the straight, longitudinal axis of the cell (i.e. the cell long axis) more often than would a more curved filament of $FtsZ^{wt}$, which prefers the circumferential axis of the cell on average. For very short filaments, these curvature preferences are so small as to become negligible,[41] as supported by the observed heterogeneity of FtsZ filament orientation by polarization microscopy.[42] However, in the case of very long filaments that may form during FtsZ overexpression, these preferences could become large enough to explain the observed expansion in Z^{D212A}-ring width that we observed upon overexpression. Another possibility could be that $FtsZ^{D212A}$ has altered lateral interactions compared to $FtsZ^{wt}$, and thus may form wider 2D sheets or bundles at the midcell. Note that in previous studies the Z^{wt}-ring width in *E. coli* cells appeared to be invariable at different cell cycle stages,[17] or when Z-ring assembly

regulators were deleted.[13,17] Thus, the observation of significantly increased width of Z^{D212A}-rings at high expression levels further demonstrates that the intrinsic GTPase activity of FtsZ, rather than other cellular factors, may determine the dimensions of the Z-ring.

As of today, our own work, together with studies from many other groups on different bacterial species, all point to a clustered, heterogeneously organized Z-ring structure under wt conditions. Here we further showed that GTPase activity of FtsZ may play an important role in modulating the Z-ring's structural organization, with higher GTPase activity leading to a more clustered, discontinuous ring organization, and lower GTPase activity leading to a smooth, continuous ring organization. We recently also showed that the chemical energy harnessed by GTP hydrolysis does not provide a mechanical, driving force limiting the rate of septum closure in *E. coli* cells.[17] It then appears that perhaps the main role of GTPase activity is to maintain the heterogeneous structural organization of the Z-ring. Furthermore, past studies have shown that many FtsZ mutants with low GTPase activities form aberrant FtsZ structures, result in abnormal cell shapes, or are unable to support cell division.[25] Overexpression of wt FtsZ can also inhibit cell division.[43] Thus it is most likely that the clustered, discontinuous Z-ring structure maintained by FtsZ's GTPase activity supports proper Z-ring function in cell division, while a homogenously distributed, continuous Z-ring structure is detrimental. Yet the biological function of this discontinuous organization remains unclear. Certainly further studies from different groups with different perspectives and methodologies will lead us closer to understanding this question, and the multi-faceted roles of FtsZ.

Acknowledgements

We thank the Xiao group members and Erin Goley group members for helpful discussions. We also thank Dr. Harold Erickson for the FtsZ antibody and Dr. Jackson Buss and Dr. Ji Yu for plasmids. This study was supported by National Institutes of Health Grant 1R01GM086447-01A2 and National Science Foundation Grant EAGER MCB1019000.

References

1. Adams, D. W.; Errington, J. Nat Rev Microbiol 2009, 7, 642-653.
2. Addinall, S. G.; Lutkenhaus, J Mol Microbiol 1996, 22, 231-237.
3. Romberg, L.; Simon, M.; Erickson, H. P. J Biol Chem 2001, 276, 11743-11753.
4. Chen, Y.; Bjornson, K.; Redick, S. D.; Erickson, H. P. Biophys J 2005, 88, 505-514.
5. Huecas, S.; Llorca, O.; Boskovic, J.; Martin-Benito, J.; Valpuesta, J. M.; Andreu, J. M. Biophys J 2008, 94, 1796-1806.
6. Mingorance, J.; Tadros, M.; Vicente, M.; Gonzalez, J. M.; Rivas, G.; Velez, M. J Biol Chem 2005, 280, 20909-20914.
7. Popp, D.; Iwasa, M.; Narita, A.; Erickson, H. P.; Maéda, Y. Biopolymers 2009, 91, 340-350.
8. Milam, S. L.; Osawa, M.; Erickson, H. P. Biophys J 2012, 103, 59-68.
9. Szwedziak, P.; Wang, Q.; Bharat, T. A.; Tsim, M.; Lowe, J. eLife 2014, 3, e04601.
10. Li, Z.; Trimble, M. J.; Brun, Y. V.; Jensen, G. J. EMBO J 2007, 26, 4694-4708.
11. Fu, G.; Huang, T.; Buss, J.; Coltharp, C.; Hensel, Z.; Xiao, J. PLoS One 2010, 5, e12682.
12. Strauss, M. P.; Liew, A. T. F.; Turnbull, L.; Whitchurch, C. B.; Monahan, L. G.; Harry, E. J. PLoS Biol 2012, 10, e1001389.
13. Buss, J.; Coltharp, C.; Huang, T.; Pohlmeyer, C.; Wang, S. C.; Hatem, C.; Xiao, J. Mol Microbiol 2013, 89, 1099-1120.
14. Holden, S. J.; Pengo, T.; Meibom, K. L.; Fernandez Fernandez, C.; Collier, J.; Manley, S. Proc Natl Acad Sci USA 2014, 111, 4566-4571.
15. Rowlett, Veronica W.; Margolin, W. Biophys J 2014, 107, L17-L20.
16. Buss, J.; Coltharp, C.; Shtengel, G.; Yang, X.; Hess, H.; Xiao, J. PLoS Genet 2015, 11, e1005128.
17. Coltharp, C.; Buss, J.; Plumer, T. M.; Xiao, J. Proc Natl Acad Sci USA 2016, 113, E1044-1053.
18. Vedyaykin, A. D.; Vishnyakov, I. E.; Polinovskaya, V. S.; Khodorkovskii, M. A.; Sabantsev, A. V. MicrobiologyOpen 2016.
19. Leisch, N.; Verheul, J.; Heindl, N. R.; Gruber-Vodicka, H. R.; Pende, N.; den Blaauwen, T.; Bulgheresi, S. Curr Biol 2012, 22, 831-832.

20. Mateos-Gil, P.; Paez, A.; Horger, I.; Rivas, G.; Vicente, M.; Tarazona, P.; Velez, M. Proc Natl Acad Sci USA 2012, 109, 8133-8138.
21. Stricker, J.; Maddox, P.; Salmon, E. D.; Erickson, H. P. Proc Natl Acad Sci USA 2002, 99, 3171-3175.
22. Oliva, M. A.; Cordell, S. C.; Lowe, J. Nat Struct Mol Biol 2004, 11, 1243-1250.
23. Nogales, E.; Downing, K. H.; Amos, L. A.; Lowe, J. Nat Structl Biol 1998, 5, 451-458.
24. Lu, C.; Stricker, J.; Erickson, H. BMC Microbiol 2001, 1, 7.
25. Stricker, J.; Erickson, H. P. J Bacteriol 2003, 185, 4796-4805.
26. Datsenko, K. A.; Wanner, B. L. Proc Natl Acad Sci USA 2000, 97, 6640-6645.
27. Rueda, S.; Vicente, M.; Mingorance, J. J Bacteriol 2003, 185, 3344-3351.
28. Pla, J.; Sanchez, M.; Palacios, P.; Vicente, M.; Aldea, M. Mol Microbiol 1991, 5, 1681-1686.
29. Mohammadi, T.; Ploeger, G. E.; Verheul, J.; Comvalius, A. D.; Martos, A.; Alfonso, C.; van Marle, J.; Rivas, G.; den Blaauwen, T. Biochemistry 2009, 48, 11056-11066.
30. Vischer, N. O. E.; Verheul, J.; Postma, M.; van den Berg van Saparoea, B.; Galli, E.; Natale, P.; Gerdes, K.; Luirink, J.; Vollmer, W.; Vicente, M.; Den Blaauwen, T. Front Microbiol 2015, 6.
31. Huang, B.; Wang, W.; Bates, M.; Zhuang, X. Science 2008, 319, 810-813.
32. Egner, A.; Hell, S. W. In Handbook of biological confocal microscopy; Springer, 2006, p 404-413.
33. Zhang, M.; Chang, H.; Zhang, Y.; Yu, J.; Wu, L.; Ji, W.; Chen, J.; Liu, B.; Lu, J.; Liu, Y.; Zhang, J.; Xu, P.; Xu, T. Nat Methods 2012, 9, 727-729.
34. Small, E.; Marrington, R.; Rodger, A.; Scott, D. J.; Sloan, K.; Roper, D.; Dafforn, T. R.; Addinall, S. G. J Mol Biol 2007, 369, 210-221.
35. Dajkovic, A.; Pichoff, S.; Lutkenhaus, J.; Wirtz, D. Mol Microbiol 2010, 78, 651-668.
36. Monahan, L. G.; Robinson, A.; Harry, E. J. Mol Microbiol 2009, 74, 1004-1017.
37. Peters, N. T.; Dinh, T.; Bernhardt, T. G. J Bacteriol 2011, 193, 4973-4983.
38. Anders, K. R.; Botstein, D. Mol Biol Cell 2001, 12, 3973-3986.
39. Coltharp, C.; Yang, X.; Xiao, J. Curr Opin Struct Biol 2014, 28, 112-121.
40. Li, Y.; Hsin, J.; Zhao, L.; Cheng, Y.; Shang, W.; Huang, K. C.; Wang, H. W.; Ye, S. Science 2013, 341, 392-395.
41. Sun, S. X.; Jiang, H. Microbiol Mol Biol Rev 2011, 75, 543-565.
42. Si, F.; Busiek, K.; Margolin, W.; Sun, Sean X. Biophys J 2013, 105, 1976-1986.
43. Erickson, H. P.; Anderson, D. E.; Osawa, M. Microbiol Mol Biol Rev 2010, 74, 504-528.

Figure Legends

Figure 1. Comparison of Z^{wt}-ring and Z^{D212A}-ring structures.

(A) Representative 3D PALM images of two-dimensional projections of live *E.coli* BW25113 cells expressing $FtsZ^{wt}$-mEos3.2 (i) or $FtsZ^{D212A}$-mEos3.2 (ii) at comparable total cellular FtsZ concentrations (~ 3 WTC). Upper, xy plane and yz plane projections. Lower, xz plane projections. Cell outlines are approximated by yellow dashed lines in the top panel, with the corresponding Z-rings outlined in dashed boxes in the panel below. The axes of a cell are defined as follows: x is the short axis of the cell parallel to the imaging plane, y is the long axis of the cell parallel to the imaging plane, and z is the axis of the cell perpendicular to the imaging plane. Scale bar, 200 nm. (B) Distributions of resolution-deconvolved width (i, bin size = 19 nm) and thickness (ii, bin size = 13 nm) of Z^{wt}-rings (black, n = 126) and Z^{D212A}-rings (red, n = 89) at ~ 3 WTC. The inset shows schematically the relative orientation of Z-ring width (i, along the cell long axis) and Z-ring thickness (ii, along the cell radius). (C) Mean spatial autocorrelation function (ACF) curves of Z^{wt}-rings (black) and Z^{D212A}-rings (red) at ~ 3 WTC averaged from all individual cells' ACFs. Error bars represent SEM.

Figure 2. Concentration dependence of Z-ring structure.

(A) Representative 3D PALM images of cropped Z-rings in cells expressing $FtsZ^{wt}$-mEos3.2 (upper) and $FtsZ^{D212A}$-mEos3.2 (lower) at increasing total cellular FtsZ concentrations. The total cellular FtsZ concentrations of cells in the same column are comparable. Scale bar, 200 nm. (B) i: Distributions of total cellular FtsZ concentrations (in WTC unit) in individual cells under both induction conditions. The four shaded areas and labels at the top indicate the grouping and average WTC unit for the four groups of cells used in this study. The number of cells and actual

mean FtsZ expression level in each group are also listed in Table S2. ii-iv: Mean spatial autocorrelation function (ACF) curves of Z^{wt}-rings (black) and Z^{D212A}-rings (red) grouped by total FtsZ concentration at ~ 5 WTC (ii, squares), ~ 8 WTC (iii, triangles), and ~ 11 WTC (iv, diamonds) respectively. For comparison, the mean ACF of simulated, homogenously distributed FtsZ molecules inside the Z-ring is shown in gray (iv, stars). Error bars represent SEM. (C) Dependence of Z-ring width (upper) and thickness (lower) of Z^{wt}-rings (black) and Z^{D212A}-rings (red) on total cellular FtsZ concentration. Width or thickness measurements from individual cells are shown as small, scattered dots with the averaged measurements from cells binned by total cellular FtsZ concentration (bin edges: 0, 4, 7, 10, and 13) plotted on top as large circles. Error bars represent SEM.

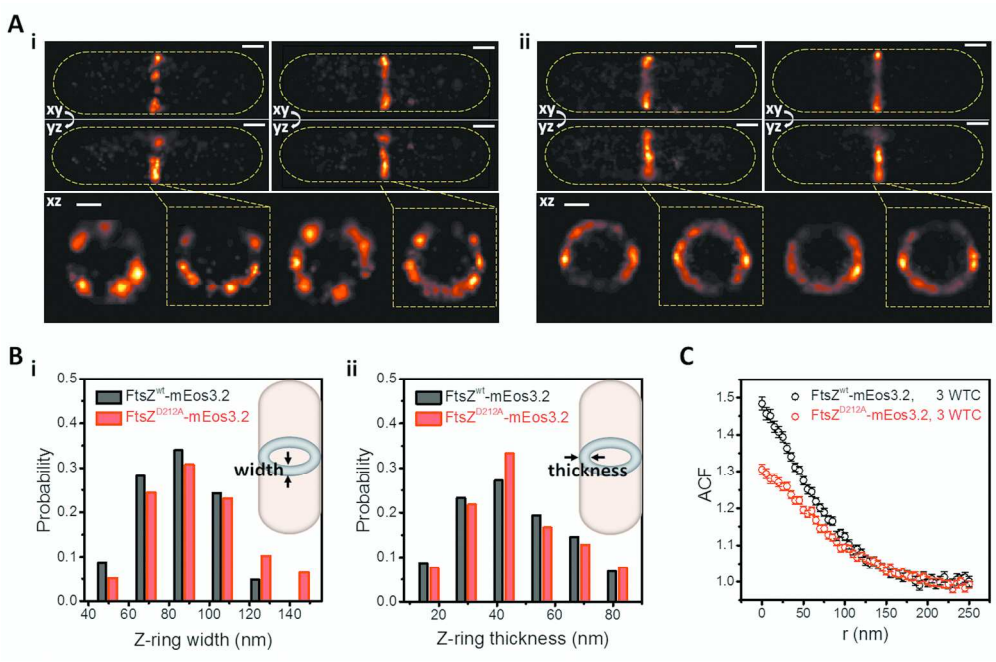

Figure 1. Comparison of Zwt-ring and ZD212A-ring structures.
(A) Representative 3D PALM images of two-dimensional projections of live E.coli BW25113 cells expressing FtsZwt-mEos3.2 (i) or FtsZD212A-mEos3.2 (ii) at comparable total cellular FtsZ concentrations (~ 3 WTC). Upper, xy plane and yz plane projections. Lower, xz plane projections. Cell outlines are approximated by yellow dashed lines in the top panel, with the corresponding Z-rings outlined in dashed boxes in the panel below. The axes of a cell are defined as follows: x is the short axis of the cell parallel to the imaging plane, y is the long axis of the cell parallel to the imaging plane, and z is the axis of the cell perpendicular to the imaging plane. Scale bar, 200 nm. (B) Distributions of resolution-deconvolved width (i, bin size = 19 nm) and thickness (ii, bin size = 13 nm) of Zwt-rings (black, n = 126) and ZD212A-rings (red, n = 89) at ~ 3 WTC. The inset shows schematically the relative orientation of Z-ring width (i, along the cell long axis) and Z-ring thickness (ii, along the cell radius). (C) Mean spatial autocorrelation function (ACF) curves of Zwt-rings (black) and ZD212A-rings (red) at ~ 3 WTC averaged from all individual cells' ACFs. Error bars represent SEM.

98x64mm (600 x 600 DPI)

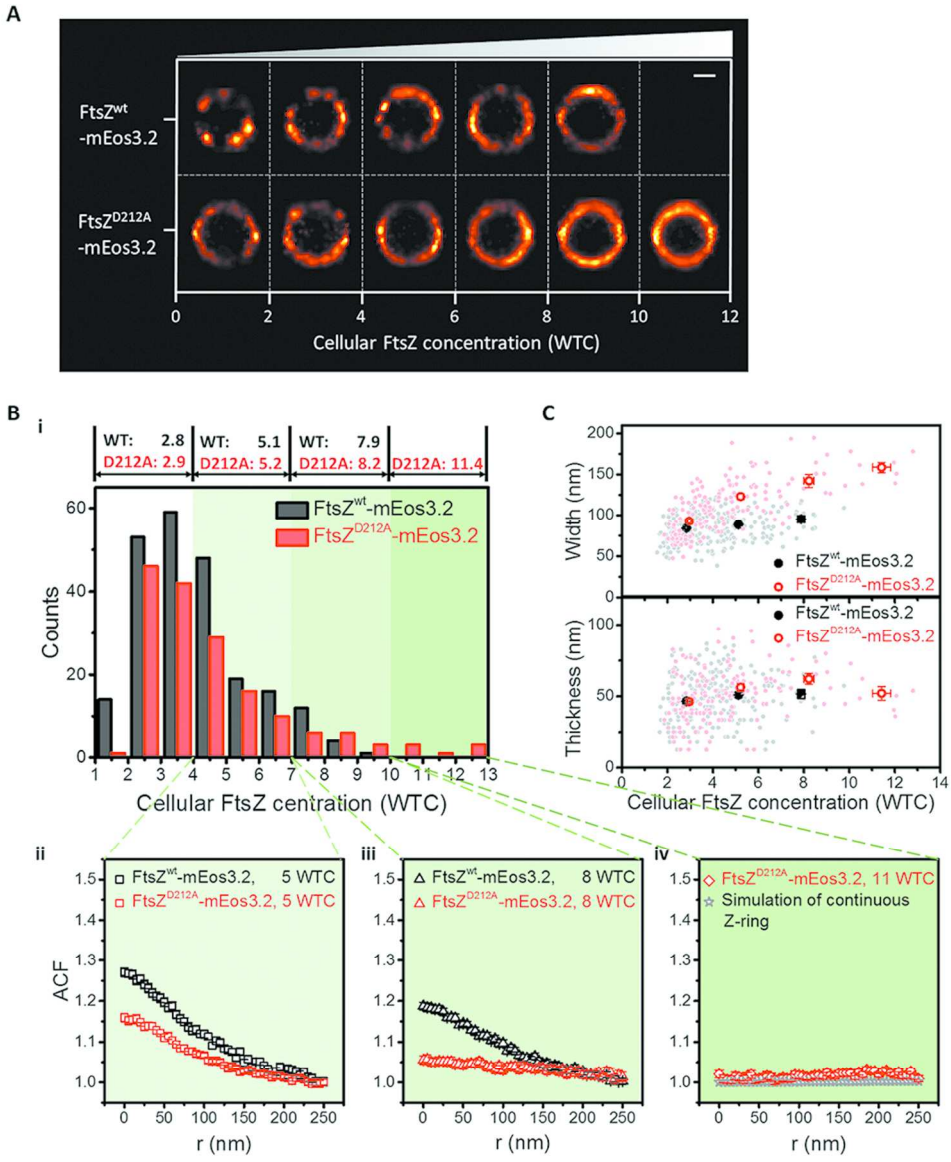

Figure 2. Concentration dependence of Z-ring structure.
(A) Representative 3D PALM images of cropped Z-rings in cells expressing FtsZwt-mEos3.2 (upper) and FtsZD212A-mEos3.2 (lower) at increasing total cellular FtsZ concentrations. The total cellular FtsZ concentrations of cells in the same column are comparable. Scale bar, 200 nm. (B) i: Distributions of total cellular FtsZ concentrations (in WTC unit) in individual cells under both induction conditions. The four shaded areas and labels at the top indicate the grouping and average WTC unit for the four groups of cells used in this study. The number of cells and actual mean FtsZ expression level in each group are also listed in Table S2. ii-iv: Mean spatial autocorrelation function (ACF) curves of Zwt-rings (black) and ZD212A-rings (red) grouped by total FtsZ concentration at ~ 5 WTC (ii, squares), ~ 8 WTC (iii, triangles), and ~ 11 WTC (iv, diamonds) respectively. For comparison, the mean ACF of simulated, homogenously distributed FtsZ molecules inside the Z-ring is shown in gray (iv, stars). Error bars represent SEM. (C) Dependence of Z-ring width (upper) and thickness (lower) of Zwt-rings (black) and ZD212A-rings (red) on total cellular FtsZ concentration. Width or thickness measurements from individual cells are shown as small, scattered dots

with the averaged measurements from cells binned by total cellular FtsZ concentration (bin edges: 0, 4, 7, 10, and 13) plotted on top as large circles. Error bars represent SEM.
124x151mm (600 x 600 DPI)